Nanoscale

PAPER

View Article Online
View Journal | View Issue

Cite this: *Nanoscale*, 2025, **17**, 21554

Wafer-scale integration of monolayer MoS_2 *via* residue-free support layer etching and angular strain suppression

Shi Wun Tong, *†[a] Mingxi Chen, †[a] Xin Ju, [a] Jianwei Chai, [a] Jun-Young Kim, [a] Jaewon Kim, [a,b] Hong Kuan Ng, [a] Benjamin Yue Hao Tan [a] and Dongzhi Chi *[a]

A crack-free and residue-free transfer technique for large-area, atomically-thin 2D transition metal dichalcogenides (TMDCs) such as MoS_2 and WS_2 is critical for their integration into next-generation electronic devices, either as channel materials replacing silicon or as back-end-of-line (BEOL) components in 3D-integrated nano-systems on CMOS platforms. However, cracks are frequently observed during the debonding of TMDCs from their growth substrates, and polymer or metal residues are often left behind after the removal of adhesive support layers *via* wet etching. These issues stem from excessive angular strain accumulated during debonding and the incomplete removal of support layers due to their low solubility. In this study, we developed a novel debonding strategy along with an optimized etching protocol to address these challenges. Characterization using Raman spectroscopy, photoluminescence (PL), X-ray photoelectron spectroscopy (XPS), atomic force microscopy (AFM), and optical microscopy (OM) confirmed that the optimized process enables clean, crack-free, and morphologically intact MoS_2 films. The success of the crack-free and residual-free transfer is attributed to two key factors: (1) the suppression of mechanical bending during debonding, which eliminates bending-induced crack formation; and (2) the precise control of etchant concentration, reaction duration, and post-etch rinsing steps, which ensures the complete removal of the support layer without damaging the MoS_2 film. Using commercially available fab tools such as wafer bonders and debonders, we successfully demonstrated the clean transfer of a 2-inch monolayer MoS_2 film with a high transfer yield of 95%, highlighting the practical applicability of this process for scalable device fabrication.

Received 21st July 2025,
Accepted 2nd September 2025

DOI: 10.1039/d5nr03068d

rsc.li/nanoscale

Introduction

Leveraging their unique thickness-dependent properties, atomically-thin two-dimensional (2D) transition metal dichalcogenides (TMDCs) have emerged as promising channel materials for ultra-scaled electronics, with potential to replace traditional silicon.[1–3] Semiconducting 2D TMDCs are also being explored for back-end-of-line (BEOL) devices in 3D-integrated nano-systems built on CMOS platforms. According to the IEEE International Roadmap for Devices and Systems (IRDS) – 2021,[4,5] high-volume manufacturing of 2D electronics is anticipated within the next decade.

In this context, large-area 2D material transfer technologies have become critical for integrating TMDCs into 3D-integrated electronics, especially since high-quality TMDCs are typically grown on lattice-matched substrates (*e.g.*, *c*-plane sapphire) at elevated temperatures incompatible with BEOL processes. Successful integration therefore hinges on two key prerequisites: (1) high-yield, damage-free detachment of TMDCs from its growth substrate, and (2) seamless, residual-free release onto the target substrate.

Among the various strategies, polymer-assisted transfer has gained widespread adoption for its conformal contact capability, substrate compatibility, and process simplicity. Poly (methyl methacrylate) (PMMA) is one of the most commonly used polymers in this approach.[6–9] However, standalone PMMA often results in contamination due to its strong adsorption onto TMDC surfaces.[10] Even after multiple lift-off or post-treatment processes,[11–13] radical sites generated during PMMA removal continue to interact strongly with TMDC surfaces, leaving behind persistent organic residues.[10] Additionally, PMMA's relatively low Young's modulus (~22 MPa)[14] provides

[a]*Institute of Materials Research and Engineering (IMRE), Agency for Science, Technology and Research (A*STAR), 2 Fusionopolis Way, Innovis #08-03, Singapore 138634, Republic of Singapore. E-mail: tongsw@imre.a-star.edu.sg, dz-chi@imre.a-star.edu.sg*
[b]*Department of Nano-devices and Displays, Korea Institute of Machinery and Materials (KIMM), Daejeon 34103, Republic of Korea*
† These authors contributed equally to this work.

insufficient mechanical support, making TMDCs vulnerable to strain-induced damage during delamination, thus reducing transfer yield.[15] The resulting cracked surfaces and increased roughness[16] caused by residual contamination have become a primary challenge in PMMA-assisted transfer,[17–20] ultimately degrading device performance due to screening effects.[21]

In this study, we address the limitations of PMMA-only assisted transfer by introducing a 30 nm thick bismuth (Bi) interlayer between PMMA and the TMDC, denoted as the PMMA/Bi-assisted transfer method. Bismuth offers sufficiently strong adhesion for detaching 2D materials and, with its high stiffness (Young's modulus ~34 GPa),[22] provides structural support that helps preserve the integrity of the transferred TMDC. Serving as an interfacial buffer, Bi is hypothesized to minimize mechanical stress during transfer. Meanwhile, PMMA remains essential as a compliant layer, ensuring conformal contact with the Bi/TMDC. Although Bi has previously shown promise as a support layer for TMDC transfer,[23] a systematic understanding of how Bi etching conditions affect the preservation of 2D material quality remains underexplored, leaving underlying chemical interactions ambiguous. In this study, we leveraged a commercially available wafer debonder to facilitate a controlled peeling process, in which the growth substrate is detached from the carrier/support layer/TMDC stack firmly mounted on the rigid bottom chuck of the debonder, while the propagation of separation front is well controlled by a programmable roller. This debonding process suppress the bending on TMDC layer, and thus substantially suppressing the angular strain imparted on the bending-free 2D TMDC to eliminate the bending-induced crack formation. This strain-minimized approach enables the preservation of monolayer crystallinity and morphology across wafer scales. Based on using this method, we demonstrate the clean transfer of a 2-inch MoS_2 film with a high yield of 95% and no observable residues.

This work showcases the residual-free TMDC transfer after the complete removal of the PMMA/Bi stack (with molybdenum disulfide, MoS_2, as a model system), emphasizing the importance of optimizing etchant concentration, etching duration, and post-treatment steps. Comprehensive characterization using Raman spectroscopy, photoluminescence (PL), X-ray photoelectron spectroscopy (XPS), atomic force microscopy (AFM), and optical microscopy (OM) confirms that the optimized PMMA/Bi-assisted process yields MoS_2 films that are clean, crack-free, and morphologically intact. Finally, wafer-scale transfer with minimal folding and wrinkling is demonstrated using existing automated fab tools (wafer bonder and debonder), highlighting the industrial compatibility of this approach.

Results and discussion

Fig. 1 shows the schematic drawings of the PMMA/Bi assisted transfer process of CVD-grown MoS_2 and the sample photos captured along different steps in the transfer. The detailed

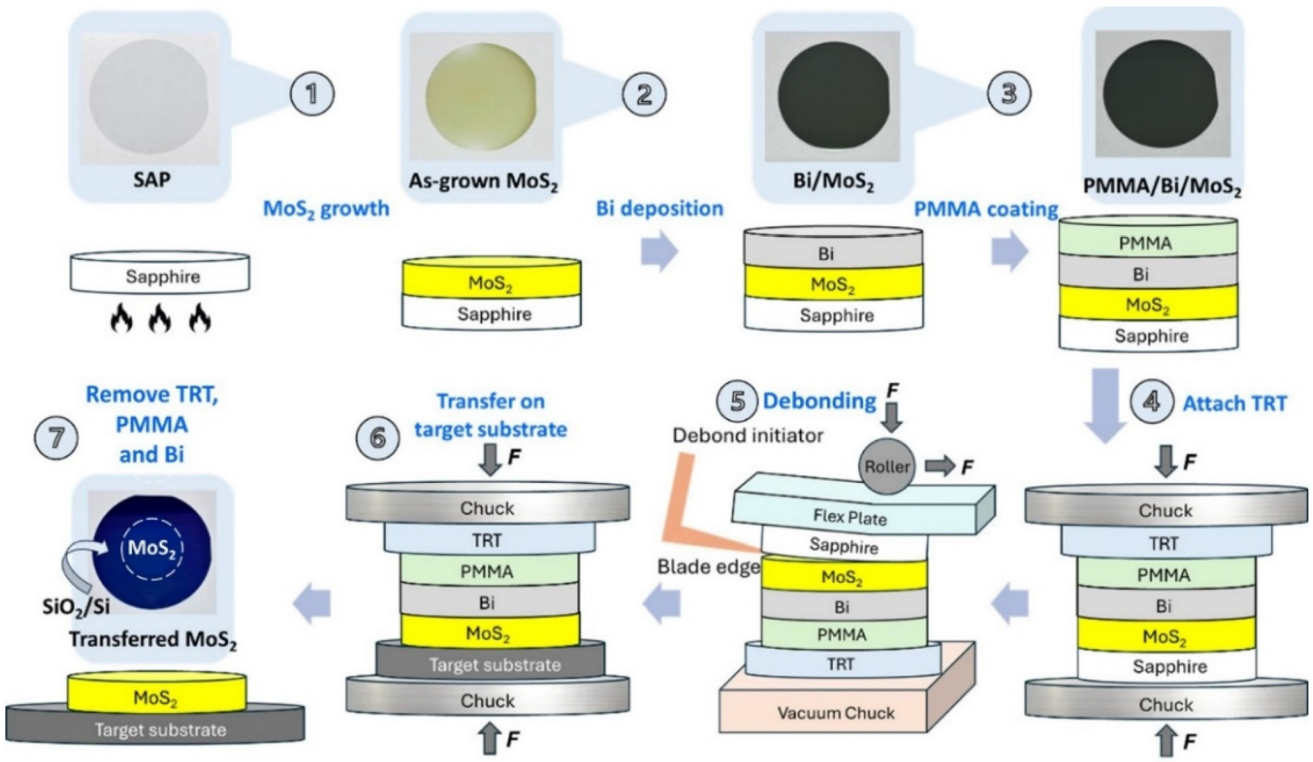

Fig. 1 Schematic drawings and photographs of samples in PMMA/Bi assisted transfer process for monolayer MoS_2.

growth and transfer procedures of MoS_2 are described in the Experimental section. Briefly, the entire process is consisted of the following steps: (1) annealing of sapphire growth substrate (SAP) at 1100 °C to promote the epitaxial growth of continuous MoS_2.[24] (2) Growth of MoS_2 on annealed SAP using a low-pressure CVD process. (3) Deposition of Bi film (30 nm) on MoS_2/SAP using e-beam evaporation. (4) Spin coating of PMMA solution (PMMA, 495 K A4, MicroChem Corp.) onto Bi/MoS_2/SAP. (5) Wafer bonding of Thermal Release Tape (TRT) with high Young's modulus (~1 GPa for the backing polyester layer of the TRT)[25] onto PMMA/Bi/MoS_2 under vacuum (~10^{-3} mbar). (6) Mechanical detachment of entire stack structure of TRT/PMMA/Bi/MoS_2 from SAP growth substrate using the wafer debonder. (7) Bonding of TRT/PMMA/Bi/MoS_2 stack onto a UV-ozone treated SiO_2/Si. (8) Removal of TRT at a temperature of 120 °C, followed by removal processes for PMMA and Bi layers *via* wet etching in acetone and nitric acid solutions, respectively, resulting in the wafer-scale transfer of MoS_2 on SiO_2/Si.

In this study, PMMA served as a compliant interfacial layer for establishing conformal contact with the underlying Bi layer,[26] as well as to alleviate adhesion issues commonly observed between rigid Bi and TRT. As such, the stack structure consisting of PMMA/Bi support and TRT carrier layers ultimately facilitates a more controlled and precise transfer process, which is particularly beneficial for scaling-up the transfer of delicate TMDCs for industrial processing.

This study achieved debonding by detaching the growth substrate from the MoS_2 monolayer, effectively reducing the angular strain on 2D material – the key technical challenge commonly encountered in previous reports.[27,28] A key distinction between our approach and the laser-assisted transfer methods reported in the literature lies in the choice of mechanical support. Instead of relying on a rigid glass carrier to support the TMDC, we mounted the carrier/support layer/TMDC stack on the bottom vacuum chuck during debonding. The high rigidity of the vacuum chuck suppresses angular deformation of the MoS_2 during debonding, thereby preserving its structural integrity and enhancing transfer yield.

During debonding (step 5 in transfer process flow in Fig. 1), the TRT/PMMA/Bi/MoS_2 stack was firmly supported from below by the vacuum chuck, while the top side of the SAP substrate was attached to a flex plate. A blade was first inserted beneath the SAP substrate to initiate delamination. Subsequently, the flex plate and SAP substrate were gradually lifted from one side under the guidance of a program-controlled roller. This roller precisely modulates the propagation of the separation front, minimizing mechanical bending and ensuring that stress on the MoS_2 remains minimal throughout the process. In addition, unlike conventional laser-assisted methods that rely on localized heating, the wafer debonder provides uniform temperature control during debonding, significantly reducing the risk of thermal gradients and defect formation in delicate 2D material. Furthermore, in contrast to laser-assisted methods that require rigid glass carriers for mechanical support and thermal expansion control, the wafer debonder-assisted process eliminates the need for such rigid carriers. This enables the use of non-rigid and flexible substrates, thereby broadening the applicability of the transfer technique to a wider range of device architectures, including those in flexible and wearable electronics.

As previously discussed, a key prerequisite for an ideal 2D material transfer is the complete detachment of MoS_2 film from its growth substrate without inducing damage. Prior studies have shown that a continuous graphene film with complete coverage and well-stitched grain boundaries can significantly facilitate clean delamination without breaking the film.[29] To achieve a facile detachment, the SAP growth substrate was annealed at 1100 °C to promote the growth of continuous MoS_2 with high coverage. As reported in our work,[24] high-temperature annealing results in atomically thin and well-defined terraces on SAP (Fig. S1, SI), serving as nucleation sites to enhance epitaxial growth of continuous and uniform MoS_2.[30–32] The entire detachment/peeling of wafer-size MoS_2 is completed within minutes *via* mechanical debonding. OM images (Fig. S2, SI) confirm that the entire regions of the 2-inch MoS_2 film were successfully and fully transferred. Although some cracks were observed near the edges of the transferred MoS_2, the overall transfer yield exceeds 95%.

Apart from promoting the growth of continuous MoS_2 film *via* substrate annealing, we further replace the conventional support layer made of standalone PMMA with a bilayer of PMMA/Bi for achieving complete MoS_2 delamination. It has been reported that a PMMA-only support layer, with a low Young's modulus of 22 MPa,[14] is unable to provide robust mechanical support for MoS_2, thereby introducing strain and thus structural damage (cracking and wrinkling) during the transfer process (Fig. 2b).[15] To overcome this, we employ an additional layer of 30 nm Bi between MoS_2 and PMMA, hereon denoted as the PMMA/Bi assisted transfer process. OM images, Raman, PL and AFM analysis are performed to compare the properties of the transferred MoS_2 using PMMA/Bi and PMMA-only support layers. In contrast to the micron-sized cracks and wrinkles observed in the PMMA-only transferred MoS_2 (Fig. 2b), the PMMA/Bi assisted transfer achieves a wrinkle-free film without visible macroscopic cracks (Fig. 2a), attributed to the high elasticity of bismuth (Young's modulus ~34 GPa).[33] The Raman spectra comparing MoS_2 samples transferred by PMMA/Bi method (black solid curve) and PMMA-only method (blue dashed curve) exhibit a peak separation (Δk) of 19.5 cm^{-1} between characteristic E_{2g} and A_{1g} modes of MoS_2 (Fig. 2c). However, a significant suppression of the PL emission at 1.87 eV is evident in the PMMA-only transferred MoS_2, whereas a stronger PL emission is observed in the PMMA/Bi transferred sample (Fig. 2d). These PL emission peaks are attributed to the A-exciton transition associated with the direct bandgap of monolayer MoS_2, and the weaker PL emission from PMMA transferred MoS_2 is due to the cracks screening excitonic transitions or introducing local electric fields that suppress radiative recombination.[6]

In an ideal 2D material transfer process, the second critical requirement is the release of the 2D material onto the target

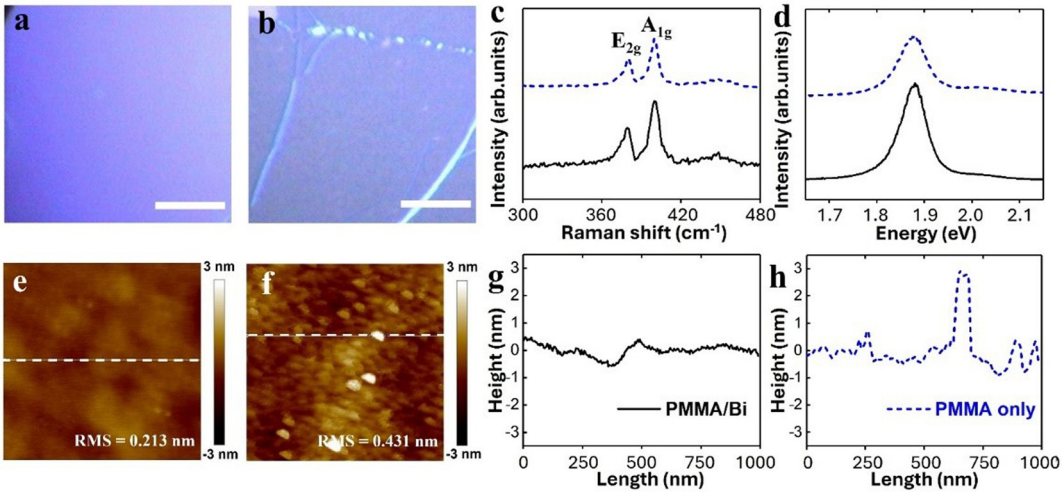

Fig. 2 (a and b) Optical microscopy images with scale bar of 10 μm. (c) Raman spectra, (d) PL spectra, (e and f) AFM topography images (1 × 1 μm), and (g and h) cross-sectional profiles taken along the location marked in (e and f), of monolayer MoS_2 after (a, c–e and g) PMMA/Bi assisted transfer and (b–d, f and h) PMMA-only assisted transfer.

substrate without introducing any residual contaminants. To achieve residue-free transfer of MoS_2, this study emphasizes the importance of selecting appropriate support layer materials and systematically investigates the effects of chemical etchants on the film's properties. As previously discussed, the conventional use of a single-layer PMMA support was replaced with a bilayer structure comprising PMMA and Bi. Complete removal of the PMMA support layer is typically achieved by immersion in an acetone bath. However, post-baking is often employed to stabilize the PMMA structure, which can lead to polymer crosslinking and subsequently reduce its solubility in acetone. Furthermore, during the dissolution of PMMA, radical sites may be generated that can interact with sulfur vacancies or defects in MoS_2, forming covalent-like bonds and resulting in persistent residues on the film surface.[34] As indicated from AFM images in Fig. 2f and h, these residues left on PMMA-only assisted transferred MoS_2 can be up to width of 30 nm and height of 3 nm which have been found to degrade contact quality and carrier mobility in 2D transistors.[35] To solve this issue, we must get rid of the strong interaction at the interface of PMMA/MoS_2. We leverage the weak interfacial interaction between Bi and TMDCs,[23] introducing a new configuration of PMMA/Bi/MoS_2, where Bi is used as an unique interfacial layer to enable transfer of residue-free MoS_2 surface, as illustrated in Fig. 2e and g. By replacing PMMA support layer with PMMA/Bi, the root mean square roughness (R_{rms}) of the MoS_2 surface is effectively reduced from 0.431 nm to 0.213 nm.

As previously noted, incomplete removal of the support layer can result in residual contamination, which adversely affects the PL emission and surface morphology of the transferred 2D material. Conversely, overly aggressive wet etching procedures may compromise the structural integrity of the atomically thin 2D layers.[36,37] Therefore, a thorough investigation into the effects of chemical etchants is essential to ensure both the preservation of the material's structure and the elimination of contaminants. Indeed, it is essential to select the mild etching conditions to ensure minimal damages on 2D material during etching (Fig. S3, SI). While precise control over etchant concentration and etching duration is critical for removing the support layer without damaging the MoS_2 film, detailed protocols for optimized etching conditions —such as the selection of mild etchants, appropriate etching times, and meticulous rinsing steps—remain scarce in the current literature.

In addition to introducing PMMA/Bi as an effective support layer for MoS_2 transfer, we present a refined etching protocol designed to completely remove the PMMA/Bi bilayer without leaving residual contamination. To evaluate the influence of etchant concentration on the quality of the transferred films, four samples consisting of PMMA/Bi/MoS_2 on SiO_2/Si substrates (each with an area of approximately 1 cm^2) were prepared for systematic analysis. PMMA was firstly removed by a conventional acetone soak (50 °C for 2 hours),[16,38–40] followed by dissolving Bi in nitric acid (HNO_3) with various concentration (0.875 wt%, 1.75 wt%, 3.5 wt% and 7 wt%) in ambient conditions for 30 minutes. Fig. 3a and b show Raman and PL spectra of MoS_2 after the PMMA/Bi removal, together with the spectrum of as-grown MoS_2 as a reference. Note that after the removal of PMMA/Bi, all transferred MoS_2 exhibit the E_{2g} peaks shift downwards by 0.1 cm^{-1}, whereas PL peaks red-shift by 0.02–0.05 eV, compared with that of as-grown MoS_2. This can be explained with the AFM images (Fig. 3c–f), which reveal substantial residue remaining on the MoS_2 surface after the removal of the PMMA/Bi. R_{rms} of all transferred MoS_2 samples ranges from 0.323 to 0.526 nm, significantly higher than that of the as-grown MoS_2 (0.22 nm, Fig. 5d), suggesting incomplete removal of the PMMA/Bi. The peak shifts in

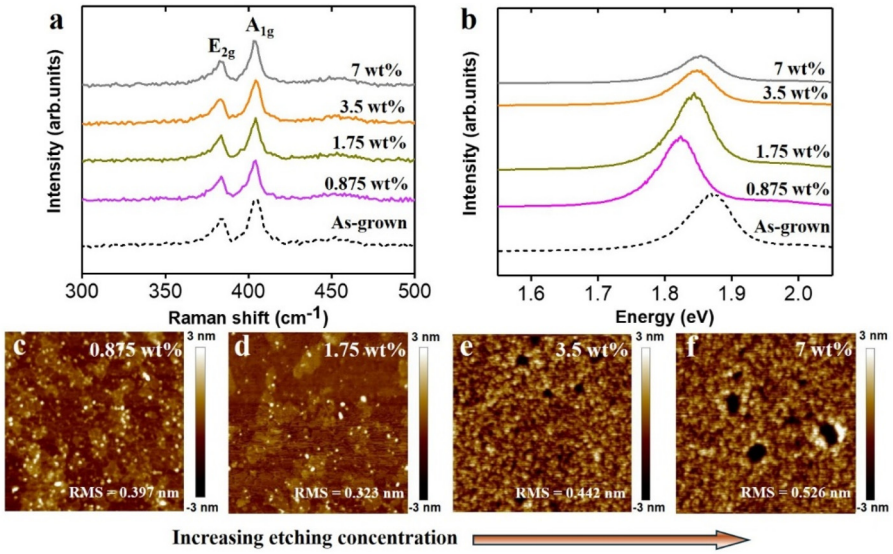

Fig. 3 (a) Raman spectra, (b) PL spectra and (c)–(f) AFM topography images (1 × 1 μm) of PMMA/Bi assisted transferred MoS_2. PMMA were dissolved in hot acetone for 2 hours, followed by the Bi etching process in nitric acid solution under various concentration (0.875 wt%, 1.75 wt%, 3.5 wt% and 7 wt%) for 30 minutes. Raman and PL properties of the as-grown MoS_2 are indicated as a reference (dashed curve in (a) and (b)).

Raman and PL of transferred MoS_2 can be caused by the doping effect of PMMA[15] and Bi residues which introduce strain into MoS_2 and thus reducing its bandgap energy.[41] In addition, we have observed that the MoS_2 being partly delaminated from the target substrate if soaking in etchant with high concentration (3.5 wt% and 7 wt% HNO_3). This observation suggests that careful control in the etching rate is essential to maintain the structural integrity of MoS_2. According to the eqn (1), Bi can react with HNO_3 to become bismuth nitrate $Bi(NO_3)_3$ with the simultaneous release of nitrogen dioxide (NO_2) gas.

$$Bi(s) + 6HNO_3(l) \rightarrow Bi(NO_3)_3(s) + 3NO_2(g) + 3H_2O(l) \quad (1)$$

Under etching in high concentration of etchant (>3.5 wt% HNO_3), the dissolution rate of Bi becomes too fast which will release lots of bubbles to induce the localized high pressure and disrupt the adhesion between MoS_2 and target substrate. Consequently, the rapid etchant diffusion rate can introduce a large mechanical stress at the interface of Bi/MoS_2 to delaminate the MoS_2.

By selecting the mild etchant (1.75 wt% HNO_3), we further optimize the etching recipe to tune the etching duration (10, 20, 40 and 60 min) in ambient as shown in Fig. 4. Under these etching conditions, E_{2g} and PL of MoS_2 still have notable peak shift though no film delamination issue is observed. For instance, extending the etching duration in 1.75 wt% HNO_3 to 40 minutes results in a slight downward shift of the E_{2g} peak by ~0.1 cm^{-1} and a redshift of the PL peak by ~0.03 eV. Simultaneously, the R_{rms} of MoS_2 decreases from 0.323 nm (30 min in 1.75 wt% HNO_3, Fig. 3d) to 0.288 nm (40 min in 1.75 wt% HNO_3, Fig. 4e), indicating improved surface cleanliness by prolonging the etching duration. However, some residues with sizes up to several tens of nanometers remain on the transferred MoS_2.

In order to further determine the origin of residues observed on all AFM images, we compare the difference in composition and morphology of as-grown MoS_2 and transferred MoS_2 by using XPS and AFM studies. As-grown MoS_2 is denoted as sample (I) in Fig. 5. Transferred MoS_2 involves the removal process of PMMA and Bi under acetone soaking and HNO_3 soaking, respectively, followed by the DI water rinsing and subsequently blown dried by N_2, denoted as sample (II) in Fig. 5. The relevant process steps used to prepare sample (II) are illustrated in Fig. 6. As shown in Fig. 5a, two sharp peaks at 229.6 and 232.7 eV corresponding to Mo $3d_{5/2}$ and Mo $3d_{3/2}$ doublet peaks of MoS_2 are well-resolved in both samples (I) and (II) in Mo 3d spectra, indicating the structural integrity of MoS_2 can be preserved after the transfer. However, extra peaks are observed from the XPS S 2p/Bi 4f of the transferred MoS_2 (sample II). Here, we have noted that S 2p of MoS_2 and Bi 4f of Bi-based compound fall along the same range of binding energy from 157–170 eV. By curve fitting with Gaussian function, the S 2p/Bi 4f spectrum of transferred MoS_2 (sample II in Fig. 5b) can be deconvoluted into four peaks: the peaks located at 162.4 and 163.6 eV are corresponding to S $2p_{3/2}$ and S $2p_{1/2}$ doublet peaks of MoS_2, while those located at 158.9 and 163.8 eV are referred to Bi $4f_{7/2}$ and Bi $4f_{5/2}$ doublet peaks of bismuth oxynitrate ($BiONO_3$).[42] Apparently, the emergence of $BiONO_3$ was caused by the transfer process, since the characteristic XPS peaks of $BiONO_3$ are absent on the as-grown sample.

As mentioned previously, Bi can be dissolved by soaking in HNO_3 to become bismuth nitrate $Bi(NO_3)_3$ (eqn (1)). According to eqn (2), we believe that the unstable by-product $Bi(NO_3)_3$ is subsequently transformed into bismuth oxynitrate ($BiONO_3$)

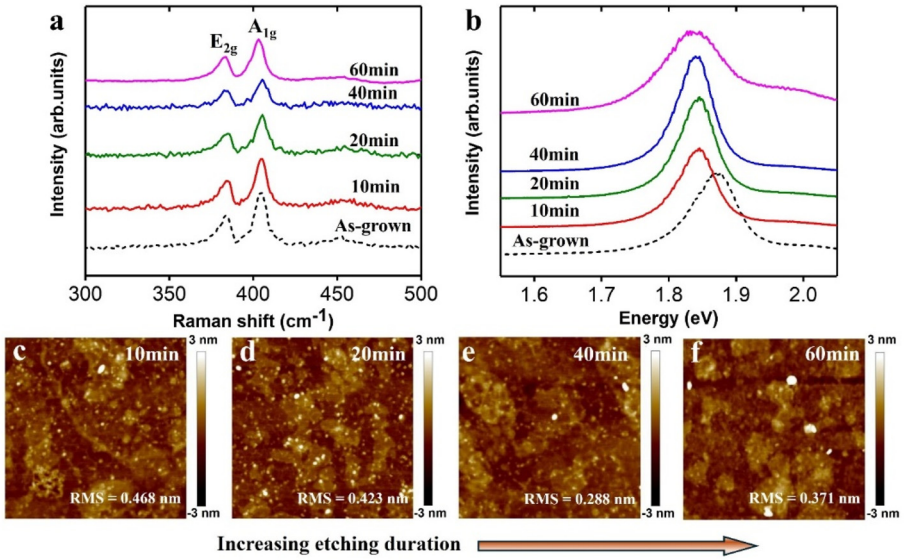

Fig. 4 (a) Raman spectra, (b) PL spectra and (c)–(f) AFM topography images (1 × 1 μm) of PMMA/Bi assisted transferred MoS_2. PMMA were dissolved in hot acetone for 2 hours, followed by the Bi etching process in 1.75 wt% nitric acid solution under various duration (10, 20, 40 and 60 minutes). Raman and PL properties of the as-grown MoS_2 are indicated as a reference (dashed curve in (a) and (b)).

under the hydrolysis in water-based HNO_3 etchant bath as shown from (II) in XPS Bi 4f spectrum.

$$Bi(NO_3)_3(s) + 2H^+(aq) + O_2(g) \rightarrow BiONO_3(s) + 5H_2O(l) \quad (2)$$

Although $BiONO_3$ is a water-soluble compound,[43] rinsing with DI water alone appears to be inadequate for its complete removal (Fig. S4 and S5, SI). We believe that one of the reasons for the incomplete removal of $BiONO_3$ is the presence of PMMA residues, which may act as a cap and hinder its dissolution in DI water. According to sample (I) in XPS C 1s (Fig. 5c), only two peaks located at 284.5 eV and 285.4 eV, which are corresponding to the C–C/C–H and C–O bondings of the atmospheric hydrocarbons respectively, can be detected from as-grown MoS_2.[44] However, an additional peak located at 288.5 eV was observed from the transferred MoS_2 marked in (II), which is attributed to O–C═O bondings of PMMA residues (Fig. S6, SI). The AFM images are consistent with the XPS data, revealing significantly different surface morphologies between the as-grown MoS_2 and the transferred MoS_2 (Fig. 5d and e). The transferred MoS_2 exhibits a significantly higher R_{rms} of 0.288 nm compared to 0.22 nm for the as-grown MoS_2, primarily due to residual $BiONO_3$ and PMMA remaining on the surface.

Although numerous studies have reported high performance in 2D material-based devices following PMMA removal *via* acetone soaking during the transfer process,[45,46] the effectiveness of this approach remains highly debated.[10,47] This controversy arises from the fact that radical sites generated during the PMMA cleaning process can strongly interact with the 2D material surface, leaving behind persistent organic residues. The size of these PMMA residues leaving after soaking in acetone can be up to micron-sized (Fig. 2f) that degrade device performance.[34] In this regard, alternative approaches based on the post-treatments such as low-temperature annealing in an inert atmosphere have shown promising effectiveness in removing persistent PMMA residues from 2D materials.[48] To ensure the complete removal of PMMA, an additional annealing step at 300 °C in N_2 is hence applied on the transferred MoS_2 followed by DI water rinsing for 30 seconds and subsequent N_2 blow-drying. The annealed sample is hereafter referred to as sample (III). Relevant process steps are depicted in Fig. 6. As intended, the annealing post-treatment effectively removes the PMMA layer and is expected to facilitate the dissolution of $BiONO_3$ during DI water rinsing.

To verify our hypothesis regarding the application of annealing to remove PMMA residues for the facile dissolution of $BiONO_3$, XPS, AFM, Raman and PL characterizations were conducted to examine the variations in composition, surface morphology, and optical properties of the transferred MoS_2 with an additional annealing step, in comparison to as-grown MoS_2. As shown in the XPS spectra of sample (III) in Fig. 5a and b, the characteristic Mo 3d and S 2p peaks of MoS_2 involved 300 °C annealing are well restored, closely matching those of the as-grown MoS_2 (sample I). The AFM image and OM image (Fig. S7, SI) of the annealed MoS_2 sample (III) further confirms the effective removal of support layer residues from the MoS_2 surface upon annealing, revealing an atomically smooth morphology with R_{rms} of 0.213 nm (Fig. 5f), which closely resembles that of the as-grown MoS_2 (0.22 nm, as shown in Fig. 5d). In terms of the optical properties of MoS_2, no significant variation is observed in the Δk of Raman peaks (Fig. 5g) and PL peak position (Fig. 5h) across the as-grown MoS_2 (sample I) and the transferred MoS_2 (sample III). Additionally, the unchanged full width at half maximum of the E_{2g} peak (~5.3 cm^{-1}), detected in both sample I and sample III, serves as a reliable indicator that the etching

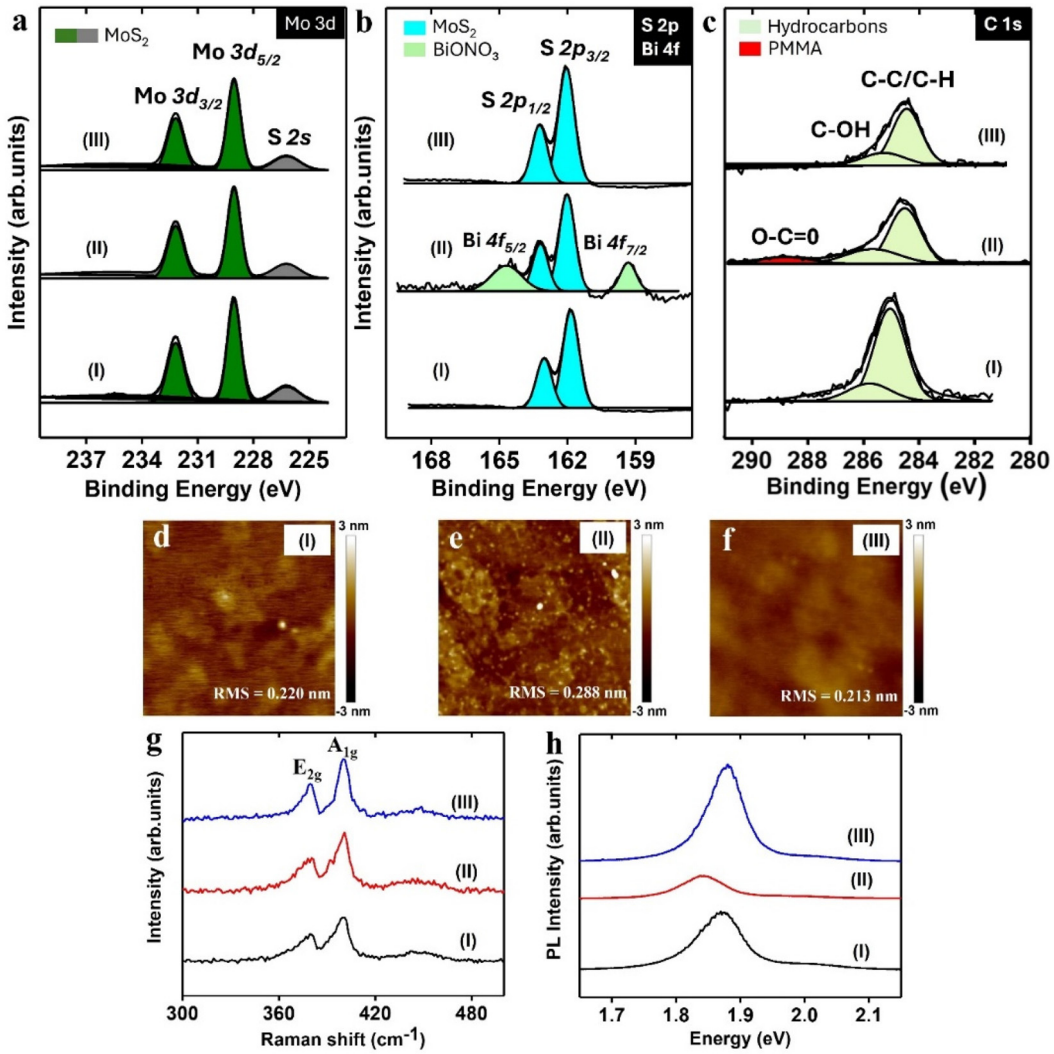

Fig. 5 Characterizations of transferred MoS_2 (sample (II) and sample (III)) after PMMA (≥99.9% acetone at 50 °C, 2 hours) and Bi etching process (1.75 wt% nitric acid, 40 minutes) with different post-treatments. XPS (a) Mo 3d, (b) S 2p, (c) C 1s, (d)–(f) AFM images, (g) Raman spectra and (h) PL spectra detected from (II) transferred MoS_2 after rinsing in DI water for 30 s, and (III) transferred MoS_2, after annealing under 300 °C for 2 hours, followed by rinsing in DI water for 30 s. Characterizations of the as-grown MoS_2 are indicated as (I) as a reference.

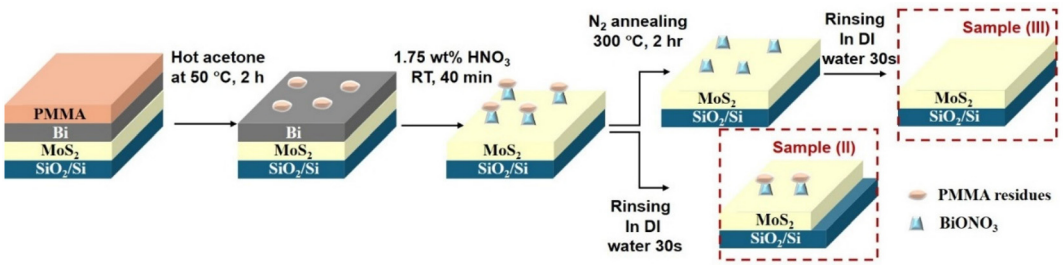

Fig. 6 Schematic drawings depict the process flow during the removal of PMMA/Bi support layer from MoS_2. After DI water rinsing, both samples (II) and (III) were subsequently dried using N_2 blow-drying.

process, post-annealing, and subsequent rinsing steps in our PMMA/Bi assisted transfer method do not compromise the crystalline quality of the MoS_2.

Lastly, we have demonstrated the high-quality transfer of wafer-sized MoS_2 based on our PMMA/Bi transfer process. Fig. 7a shows the photograph of 2-inch MoS_2 film transferred

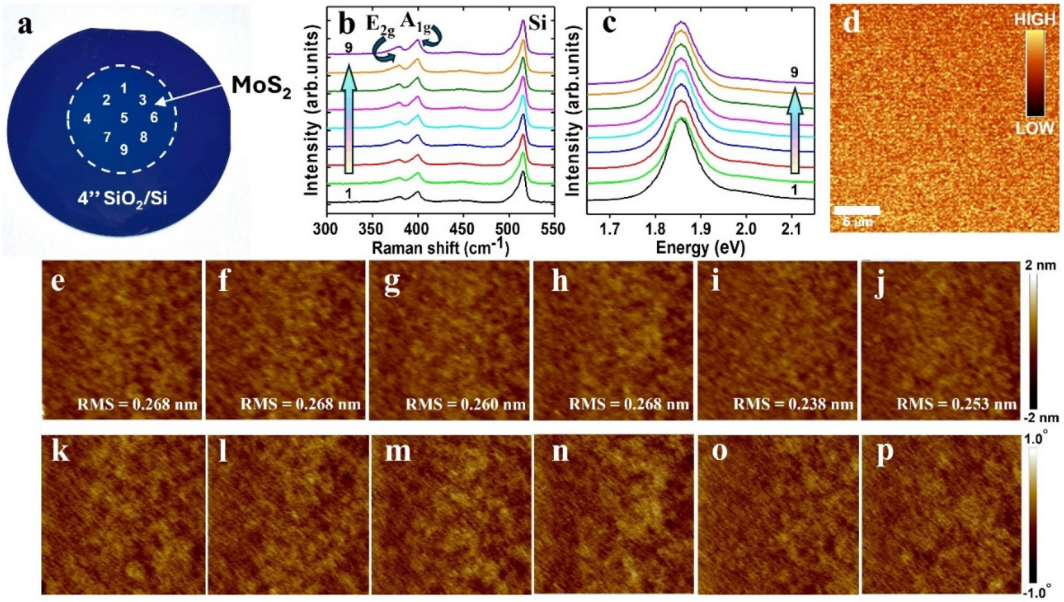

Fig. 7 (a) Photograph of 2'' MoS_2 transferred onto 4'' SiO_2/Si substrate under PMMA/Bi assisted transfer. (b) Raman and (c) PL spectra of MoS_2 film measured from 9 different spots as indicated in (a). (d) Mapping image showing the uniformity of PL intensity captured from MoS_2 (30 × 30 μm). (e)–(j) AFM topography images and (k)–(p) corresponding phase images (10 × 10 μm) of MoS_2 film measured from spots 1 to 6.

onto 4-inch SiO_2/Si substrate. Raman, PL and AFM measurements were performed on different regions of the MoS_2 film to assess the Raman modes, PL emission and surface morphology on the corresponding positions and analyze their area uniformity across the 2-inch MoS_2. Fig. 7b and c compares the Raman modes and PL properties obtained on different regions on the wafer, respectively. No noticeable variations in peak positions and intensities are observed for the two signature Raman peaks, E_{2g} and A_{1g}. Furthermore, the emission intensity of the PL peak essentially remains the same for the different positions on the wafer. Both Raman and PL properties indicate the excellent uniformity of the MoS_2 film transferred on the SiO_2/Si wafer. Fig. 7d shows the mapping image of the PL peak intensity captured from central region of the transferred MoS_2. The homogeneous color contrast shown from the mapping image suggests that the transferred MoS_2 film maintains a high degree of integrity with minimum defects. The high uniformity of MoS_2 film is further confirmed by AFM topography images (Fig. 7e–j) where R_{rms} as low as 0.26 nm are obtained with minimal phase shifts in phase images (Fig. 7k–p).

Besides, we have developed a new debonding process to suppress the bending on TMDC layer, and thus substantially suppressing the angular strain imparted on the bending-free 2D TMDC to eliminate the bending-induced crack formation. Coupled with the systematic optimization of the Bi etching parameters—including etchant concentration, etching duration, and post-transfer treatments—we demonstrate the excellent preservation of the optical and morphological integrity of the transferred MoS_2 films. This well-defined etching protocol enables consistent and reproducible transfer quality across different research laboratories and fabrication environments, which is essential for benchmarking material performance. The resulting wafer-scale MoS_2 films are crack-free and residue-free, retaining the original optical, structural, and morphological characteristics of the as-grown monolayer, as confirmed by Raman, PL, XPS, AFM, and OM. Notably, the successful integration of automated wafer bonding tools into the process highlights the scalability and manufacturing compatibility of this approach, paving the way for reliable 2D material integration in advanced electronic and optoelectronic applications.

Conclusions

In summary, the PMMA/Bi-assisted transfer strategy effectively overcomes the limitations associated with conventional PMMA-only methods for transferring two-dimensional (2D) MoS_2. The introduction of a mechanically robust bismuth (Bi) interlayer provides enhanced structural support during delamination while simultaneously reducing interfacial adhesion to MoS_2, thereby minimizing polymer residue contamination.

Method

Chemical vapor deposition growth of monolayer MoS_2 on annealed *c*-plane sapphire

MoS_2 was grown on *c*-plane (0001) sapphire (SAP) based on our previous optimized CVD process using Ni foam (NiO foam) barrier.[24] Prior to the growth, SAP was annealed at 1100 °C for 1 h in air to attain well-aligned atomically flat terraces (Fig. S1, SI) on its surface which promotes the growth of epitaxial MoS_2

grains on SAP. The SAP substrate was then placed inside a single open-end cylindrical tube containing the 3.5 mg of MoO_3 precursor and sulfurized with 1.5 g of S precursor in a two-zone CVD reactor at a temperature of 750 °C. The entire growth process was undergone at a pressure of 6 Torr for 10 minutes under an argon gas flow of 50 sccm. The system was allowed to cool naturally to 600 °C before opening the furnace hatch for rapid cooling.

Dry transfer process of 2-inch MoS_2 using PMMA/Bi support layer

Debonding from sapphire using wafer debonder. First, 30 nm Bi was deposited on MoS_2/SAP by e-beam evaporation at $\sim 6 \times 10^{-6}$ Torr (note: e-beam evaporation of Bi under a moderate vacuum could suppress defect generation and preserve the intrinsic properties of MoS_2; see Fig. S8, SI). PMMA solution (PMMA, 495 K A4, MicroChem Corp.) was secondly spin-coated onto Bi/MoS_2/SAP sample at a spinning speed of 500 rpm for 10 s, followed by 3000 rpm for 60 s. The PMMA adhered along the edge of PMMA/Bi/MoS_2/SAP stack was gently removed by a cotton bud before drying. The sample was left to dry in a fume hood overnight. To improve the adhesion at the interface, the TRT (REVALPHA 3195MS) was pressed onto the PMMA/Bi/MoS_2/SAP stack under vacuum ($\sim 1 \times 10^{-3}$ bar) by employing the wafer bonder (EVG®510). Subsequently, the entire stack structure of TRT/PMMA/Bi/MoS_2 was mechanically detached from the sapphire by using the wafer debonder (DB12T) at a controlled speed of 0.3 mm s^{-1}.

Bonding onto SiO_2/Si using wafer bonder. Prior to the bonding, the target substrate made of 300 nm SiO_2/Si was exposed to UV ozone for 10 minutes to eliminate any organic residues. After the ozone treatment, the TRT/PMMA/Bi/MoS_2 stack was placed on top of SiO_2/Si inside the wafer bonder and kept in vacuum ($\sim 1 \times 10^{-3}$ bar) for 6 hours to remove any moisture on the surfaces. The wafer bonder (EVG®510) was then employed to apply vacuum bonding TRT/PMMA/Bi/MoS_2 onto SiO_2/Si for 1 hour. Afterwards, the TRT was released by heating the sample on a hotplate at a temperature of 120 °C under ambient conditions. The sample was then soft baked at 180 °C for 1 h to improve adhesion between MoS_2 and SiO_2/Si.

Removal of PMMA/Bi support layer from PMMA/Bi/MoS_2/SiO_2/Si. PMMA was removed from the delaminated PMMA/Bi/MoS_2/SiO_2/Si using ≥99.9% acetone bath at temperature of 50 °C for 2 hours, followed by the IPA rinsing and blowing dry with nitrogen gas. Subsequently, Bi was removed by immersing the sample in 1.75 wt% HNO_3 etchant solution bath at room temperature for 40 minutes. Afterwards, the sample was rinsed under a gentle DI H_2O stream, followed by blowing dry with N_2 gun. The sample was then annealed at 300 °C for 2 hours in a nitrogen atmosphere (flow rate of 100 sccm) at a pressure of 0.1 Torr. Finally, the sample was rinsed in DI H_2O under ambient conditions for 30 s and dried overnight.

Dry transfer process of 2-inch MoS_2 using PMMA support layer

PMMA solution (PMMA, 495 K A4, MicroChem Corp.) was firstly spin-coated onto MoS_2/SAP sample at a spinning speed of 500 rpm for 10 s, followed by 3000 rpm for 60 s. The PMMA adhered along the edge of PMMA/MoS_2/SAP stack was gently removed by a cotton bud before drying. The sample was left to dry in a fume hood overnight. To improve the adhesion at the interface, the TRT (REVALPHA 3195MS) was pressed onto the PMMA/MoS_2/SAP stack under vacuum ($\sim 1 \times 10^{-3}$ bar) by employing the wafer bonder (EVG®510). A small portion (approximately 10% of total area) of TRT/PMMA/MoS_2 was then immersed into DI water at an angle of ~45° with respect to the water surface for 1 hour, followed by blowing dry with N_2 gas. Subsequently, the entire stack structure of TRT/PMMA/MoS_2 was mechanically detached from the sapphire by using the wafer debonder (DB12T) at a controlled speed of 0.3 mm s^{-1}.

Prior to the bonding, the target substrate made of 300 nm SiO_2/Si was exposed to UV ozone for 10 minutes to eliminate any organic residues. After the ozone treatment, both of SiO_2/Si and the TRT/PMMA/MoS_2 stack was placed inside the wafer bonder and kept in vacuum ($\sim 1 \times 10^{-3}$ bar) for 6 hours to remove any moisture on the surfaces. The wafer bonder (EVG®510) was then employed to apply vacuum bonding TRT/PMMA/MoS_2 onto SiO_2/Si for 1 hour. Afterwards, the TRT was released by heating the sample on a hotplate at a temperature of 120 °C under ambient conditions. The sample was then soft baked at 180 °C for 1 h to improve adhesion between MoS_2 and SiO_2/Si. PMMA was removed from the delaminated PMMA/MoS_2/SiO_2/Si using ≥99.9% acetone bath at temperature of 50 °C for 2 hours, followed by the IPA rinsing and blowing dry with nitrogen gas. The sample was then annealed at 300 °C for 2 hours in a nitrogen atmosphere (flow rate of 100 sccm) at a pressure of 0.1 Torr.

Materials characterization

Raman and photoluminescence (PL) data were acquired with laser excitation at 532 nm using a WiTEC system. With a 100× objective lens (NA = 0.9), 1800 and 600 gratings per mm were used for Raman and PL measurement respectively at room temperature. Note that the Si peak at 520 cm^{-1} was used for calibration in the experiments. For other structural characterization, Bruker dimension FastScan atomic force microscope were used to capture tapping-mode AFM images of MoS_2. XPS measurements were achieved using a monochromatic Al Kα source in an ultrahigh vacuum VG ESCALAB 220i-XL system. All XPS spectra were aligned with the C 1s reference peak at 284.6 eV to compensate the sample charging effect.

Author contributions

S. W. Tong: conceptualization, methodology, investigation, writing – original draft. M. C.: resources. J. C., X. J., J.-Y. K., J. K., H. K. Ng, B. T. Y. H.: investigation, data curation. D. C.: supervision and validation. All authors reviewed, edited, and approved the manuscript.

Conflicts of interest

There are no conflicts to declare.

Data availability

The data supporting this article have been included as part of the SI.

Supplementary information is available. See DOI: **https://doi.org/10.1039/d5nr03068d**.

Acknowledgements

This research is supported by the National Research Foundation, Singapore, under its Competitive Research Program (NRF-CRP24-2020-0002).

References

1 A. Quellmalz, X. Wang, S. Sawallich, B. Uzlu, M. Otto, S. Wagner, Z. Wang, M. Prechtl, O. Hartwig, S. Luo, G. S. Duesberg, M. C. Lemme, K. B. Gylfason, N. Roxhed, G. Stemme and F. Niklaus, *Nat. Commun.*, 2021, **12**, 917.
2 U. Celano, D. Schmidt, C. Beitia, G. Orji, A. V. Davydov and Y. Obeng, *Nanoscale Adv.*, 2024, **6**, 2260–2269.
3 J. H. Cha, I. Lee, S. W. Yun, W. Hong, H. H. Byeon, J. Oh, S. Park and S. Y. Choi, *Nanoscale*, 2025, **17**, 11305–11315.
4 *The IEEE International Roadmap For Devices And Systems: Beyond CMOS.* 2021.
5 *The IEEE International Roadmap For Devices And Systems: Metrology.* 2021.
6 P. V. Pham, T. H. Mai, S. P. Dash, V. Biju, Y. L. Chueh, D. Jariwala and V. Tung, *ACS Nano*, 2024, **18**, 14841–14876.
7 M. Nakatani, S. Fukamachi, P. Solís-Fernández, S. Honda, K. Kawahara, Y. Tsuji, Y. Sumiya, M. Kuroki, K. Li, Q. Liu, Y.-C. Lin, A. Uchida, S. Oyama, H. G. Ji, K. Okada, K. Suenaga, Y. Kawano, K. Yoshizawa, A. Yasui and H. Ago, *Nat. Electron.*, 2024, **7**, 119–130.
8 B. Yu, S. Wu, J. Li and Z. Li, *Adv. Mater. Technol.*, 2025, **10**, 2500697.
9 D. Y. Park, H. C. Suh, S. Bang, J. C. Lee, J. Yoo, H. Ko, S. H. Choi, K. K. Kim, S. M. Lee, S. C. Lim, T. U. Nahm and M. S. Jeong, *Nanoscale*, 2024, **16**, 10779–10788.
10 Y. C. Lin, C. C. Lu, C. H. Yeh, C. Jin, K. Suenaga and P. W. Chiu, *Nano Lett.*, 2012, **12**, 414–419.
11 Z. Cheng, Q. Zhou, C. Wang, Q. Li, C. Wang and Y. Fang, *Nano Lett.*, 2011, **11**, 767–771.
12 N. Peltekis, S. Kumar, N. McEvoy, K. Lee, A. Weidlich and G. S. Duesberg, *Carbon*, 2012, **50**, 395–403.
13 J. H. Park, W. Jung, D. Cho, J. T. Seo, Y. Moon, S. H. Woo, C. Lee, C. Y. Park and J. R. Ahn, *Appl. Phys. Lett.*, 2013, **103**, 171609.
14 W. Hu, D. Antoine and X. Yu, *J. Compos. Mater.*, 2013, **48**, 3019–3024.
15 S. Lai, J. Jeon, Y.-J. Song and S. Lee, *RSC Adv.*, 2016, **6**, 57497–57501.
16 Q. H. Thi, H. Kim, J. Zhao and T. H. Ly, *npj 2D Mater. Appl.*, 2018, **2**, 34.
17 A. J. Watson, W. Lu, M. H. D. Guimarães and M. Stöhr, *2D Mater.*, 2021, **8**, 032001.
18 Y. Wang, J. C. Kim, R. J. Wu, J. Martinez, X. Song, J. Yang, F. Zhao, A. Mkhoyan, H. Y. Jeong and M. Chhowalla, *Nature*, 2019, **568**, 70–74.
19 J. Shim, S. H. Bae, W. Kong, D. Lee, K. Qiao, D. Nezich, Y. J. Park, R. Zhao, S. Sundaram, X. Li, H. Yeon, C. Choi, H. Kum, R. Yue, G. Zhou, Y. Ou, K. Lee, J. Moodera, X. Zhao, J. H. Ahn, C. Hinkle, A. Ougazzaden and J. Kim, *Science*, 2018, **362**, 665–670.
20 S. H. Bae, X. Zhou, S. Kim, Y. S. Lee, S. S. Cruz, Y. Kim, J. B. Hannon, Y. Yang, D. K. Sadana, F. M. Ross, H. Park and J. Kim, *Proc. Natl. Acad. Sci. U. S. A.*, 2017, **114**, 4082–4086.
21 A. Mondal, C. Biswas, S. Park, W. Cha, S. H. Kang, M. Yoon, S. H. Choi, K. K. Kim and Y. H. Lee, *Nat. Nanotechnol.*, 2024, **19**, 34–43.
22 J. Kokorian, J. B. C. Engelen, J. de Vries, H. Nazeer, L. A. Woldering and L. Abelmann, *Thin Solid Films*, 2014, **550**, 298–304.
23 M.-Y. Li, C.-H. Hsu, S.-W. Shen, A.-S. Chou, Y. C. Lin, C.-P. Chuu, N. Yang, S.-A. Chou, L.-Y. Huang, C.-C. Cheng, W.-Y. Woon, S. Liao, C.-I. Wu, L.-J. Li, I. Radu, H. S. P. Wong and H. Wang, Presented in part at the 2022 IEEE Symposium on VLSI Technology and Circuits (VLSI Technology and Circuits), 2022.
24 X. Feng, S. Li, S. L. Wong, S. Tong, L. Chen, P. Zhang, L. Wang, X. Fong, D. Chi and K. W. Ang, *ACS Nano*, 2021, **15**, 1764–1774.
25 Y. C. Shen, B. K. Wu, T. S. Tsai, M. Liu, J. H. Chen, T. Y. Yang, R. H. Cyu, C. T. Chen, Y. C. Hsu, C. H. Luo, Y. Q. Huang, Y. R. Peng, C. H. Shen, Y. F. Lin, P. W. Chiu, Y. C. King and Y. L. Chueh, *Small Sci.*, 2024, **4**, 2300144.
26 C. Kim, M.-A. Yoon, B. Jang, H.-D. Kim, J.-H. Kim, A. T. Hoang, J.-H. Ahn, H.-J. Jung, H.-J. Lee and K.-S. Kim, *NPG Asia Mater.*, 2021, **13**, 44.
27 C. Huyghebaert, T. Schram, Q. Smets, T. Kumar Agarwal, D. Verreck, S. Brems, A. Phommahaxay, D. Chiappe, S. El Kazzi, C. Lockhart de la Rosa, G. Arutchelvan, D. Cott, J. Ludwig, A. Gaur, S. Sutar, A. Leonhardt, D. Marinov, D. Lin, M. Caymax, I. Asselberghs, G. Pourtois and I. P. Radu, 2018, *IEEE International Electron Devices Meeting (IEDM)*, 2018, pp. 22.21.21–22.21.24.
28 Q. S. S. Ghosh, S. Banerjee, T. Schram, K. Kennes, R. Verheyen, P. Kumar, M.-E. Boulon, B. Groven, H. M. Silva, S. Kundu, D. Cott, D. Lin, P. Favia, T. Nuytten, A. Phommahaxay, I. Asselberghs, C. de la Rosa, G. S. Kar and S. Brems, *2023 IEEE Symposium on VLSI Technology and Circuits (VLSI Technology and Circuits)*, 2023, pp. 1–2.
29 M. Seol, M. H. Lee, H. Kim, K. W. Shin, Y. Cho, I. Jeon, M. Jeong, H. I. Lee, J. Park and H. J. Shin, *Adv. Mater.*, 2020, **32**, e2003542.
30 T. Isono, T. Ikeda, R. Aoki, K. Yamazaki and T. Ogino, *Surf. Sci.*, 2010, **604**, 2055–2063.
31 S. Y. Kim, Z. Sun, J. Roy, X. Wang, Z. Chen, J. Appenzeller and R. M. Wallace, *ACS Appl. Mater. Interfaces*, 2024, **16**, 54790–54798.

32 L Kang, D. Tian, L. Meng, M. Du, W. Yan, Z. Meng and X. a. Li, *Surf. Sci.*, 2022, **720**, 122046.
33 J. Toudert, R. Serna, C. Deeb and E. Rebollar, *Opt. Mater. Express*, 2019, **9**, 2924.
34 R. Tilmann, C. Bartlam, O. Hartwig, B. Tywoniuk, N. Dominik, C. P. Cullen, L. Peters, T. Stimpel-Lindner, N. McEvoy and G. S. Duesberg, *ACS Nano*, 2023, **17**, 10617–10627.
35 H. J. Chuang, B. Chamlagain, M. Koehler, M. M. Perera, J. Yan, D. Mandrus, D. Tomanek and Z. Zhou, *Nano Lett.*, 2016, **16**, 1896–1902.
36 Z.-Q. Xu, Y. Zhang, S. Lin, C. Zheng, Y. L. Zhong, X. Xia, Z. Li, P. J. Sophia, M. S. Fuhrer, Y.-B. Cheng and Q. Bao, *ACS Nano*, 2015, **9**, 6178–6187.
37 K. Kang, S. Xie, L. Huang, Y. Han, P. Y. Huang, K. F. Mak, C. J. Kim, D. Muller and J. Park, *Nature*, 2015, **520**, 656–660.
38 K. Kang, K. H. Lee, Y. Han, H. Gao, S. Xie, D. A. Muller and J. Park, *Nature*, 2017, **550**, 229–233.
39 S. M. Shinde, T. Das, A. T. Hoang, B. K. Sharma, X. Chen and J. H. Ahn, *Adv. Funct. Mater.*, 2018, **28**, 1706231.
40 P. Pransisco, *IOP Conf. Ser.: Mater. Sci. Eng.*, 2019, **539**, 012009.
41 Z. Lin, Y. Zhao and C. Zhou, *Sci. Rep.*, 2016, **5**, 18596.
42 G. Pellegrino, G. Mineo, V. Strano, G. Marcellino, L. Pulvirenti, F. Ursino, S. Mirabella and G. G. Condorelli, *Colloids Surf., A*, 2025, **705**, 135738.
43 ChemBK.com, bismuth nitrate($Bi(NO_3)_3$), **https://www.chembk.com/en/chem/Bismuth%20nitrate(Bi(NO3)3)**.
44 A. Nahar, M. A. Akbor, N. S. Pinky, N. J. Chowdhury, S. Ahmed, M. A. Gafur, U. S. Akhtar, M. S. Quddus and F. Chowdhury, *Heliyon*, 2023, **9**, e17793.
45 Y. Zhao, Y. Song, Z. Hu, W. Wang, Z. Chang, Y. Zhang, Q. Lu, H. Wu, J. Liao, W. Zou, X. Gao, K. Jia, L. Zhuo, J. Hu, Q. Xie, R. Zhang, X. Wang, L. Sun, F. Li, L. Zheng, M. Wang, J. Yang, B. Mao, T. Fang, F. Wang, H. Zhong, W. Liu, R. Yan, J. Yin, Y. Zhang, Y. Wei, H. Peng, L. Lin and Z. Liu, *Nat. Commun.*, 2022, **13**, 4409.
46 T. F. Schranghamer, M. Sharma, R. Singh and S. Das, *Chem. Soc. Rev.*, 2021, **50**, 11032–11054.
47 Y. Ahn, H. Kim, Y.-H. Kim, Y. Yi and S.-I. Kim, *Appl. Phys. Lett.*, 2013, **102**, 091602.
48 B. Zhuang, S. Li, S. Li and J. Yin, *Carbon*, 2021, **173**, 609–636.